

ARTICLE

DOI: 10.1038/s42005-018-0062-z

OPEN

Dislocation avalanche mechanism in slowly compressed high entropy alloy nanopillars

Yang Hu^{1,2}, Li Shu³, Qun Yang^{1,2}, Wei Guo⁴, Peter K. Liaw⁵, Karin A. Dahmen³ & Jian-Min Zuo 1,2

Crystals deform by the intermittent multiplication and slip avalanches of dislocations. While dislocation multiplication is well-understood, how the avalanches form, however, is not clear, and the lack of insight in general has contributed to "a mass of details and controversy" about crystal plasticity. Here, we follow the development of dislocation avalanches in the compressed nanopillars of a high entropy alloy, Al_{0.1}CoCrFeNi, using direct electron imaging and precise mechanical measurements. Results show that the avalanche starts with dislocation accumulations and the formation of dislocation bands. Dislocation pileups form in front of the dislocation bands, whose giveaway trigs the avalanche, like the opening of a floodgate. The size of dislocation avalanches ranges from few to 10² nm in the nanopillars, with the power-law distribution similar to earthquakes. Thus, our study identifies the dislocation interaction mechanism for large crystal slips, and provides critical insights into the deformation of high entropy alloys.

1

¹Department of Materials Science and Engineering, University of Illinois at Urbana-Champaign, 1304 W Green St, Urbana, IL 61801, USA. ² Fredrick Seitz Materials Research Laboratory, University of Illinois at Urbana-Champaign, 104 S Goodwin Ave, Urbana, IL 61801, USA. ³ Department of Physics, University of Illinois at Urbana-Champaign, 1110 West Green Street, Urbana, IL 61801, USA. ⁴ Center for Nanophase Materials Sciences, Oak Ridge National Laboratory, P.O. Box 2008, Oak Ridge, TN 37831, USA. ⁵ Department of Materials Science and Engineering, The University of Tennessee, 1508 Middle Drive, Knoxville, TN 37996, USA. Correspondence and requests for materials should be addressed to J.-M.Z. (email: jianzuo@illinois.edu)

ecent research efforts have focused on intermittency in crystal plasticity. For example, acoustic emissions from stressed ice revealed discrete dislocation avalanches, whose magnitudes follow a power-law distribution^{1,2}. Mechanical testing on microcrystals detected sudden strain bursts^{3,4}, which also follow the power-law scaling between the number of bursts and their magnitudes⁴⁻⁷. Together, these experiments convincingly demonstrated criticality among relatively large and rapid dislocation events. On the other hand, the fundamental operating units in crystal plasticity are individual dislocations²⁻⁴. There is a long history of transmission electron microscopy (TEM) studies of dislocations and their interaction mechanisms^{8–10}, which have also revealed complex dislocation patterns in deformed crystals, including dislocation cells¹¹ and persistent slip bands¹². However, how intermittent dislocation activities stem from complex dislocation patterns, how these activities impact the dislocation pattern formation, and how this trend leads to crystal slip, are all unresolved critical questions^{5,13,14}.

To start addressing these questions, we followed the dislocation motions inside a slowly compressed nanopillars using the brightfield (BF) TEM, while simultaneously we measured the load and displacement using a pico-indenter (model PI 95, Hysitron, MN, USA). Together, these two measurements enabled us to detect a broad range of dislocation motions from few nm/s to hundreds of μm/s. For the material, we focused on high entropy alloys (HEAs), composed of five or more elements of near-equal molar percentages in nearly-random solutions^{15–18}. HEAs are promising materials for their excellent thermomechanical properties¹⁹. Previous studies also demonstrated unexplained mechanical behaviors in HEAs, including sudden stress drops or "serrations" in the stress-strain curves of bulk samples 20. The HEA of Al_{0.1}CoCrFeNi studied here has a simple fcc structure, but because of the differences in atomic radii, the material exhibits severe lattice distortions^{17,21}, providing a complex dislocationpinning landscape.

Here, we show that dislocations accumulate and are stored in the HEA nanopillars in a manner opposite to mobile dislocation starvation^{6,22,23}. Dislocation storage leads to the formation of dislocation bands and dislocation pileups in front of the band. The dislocation band propagates intermittently along the compression direction through dislocation slips. The avalanche mechanism that we identified is based on interactions between the dislocation pileup and the dislocation band, and between the pileup and dislocation pinning centers.

Results

Deformation of the HEA nanopillar. The experimental design to observe dislocation avalanches is shown in Fig. 1a using a TEM nanoindenter holder. A nanopillar is deformed by compression. The deformation process is simultaneously observed by electron imaging and the measurement of load and displacement, which are used to calculate the stress and strain in the nanopillar. An asprepared nanopillar is imaged in Fig. 1b using the BF TEM. The composition and structure of the HEA sample were characterized by atom probe tomography (APT), electron imaging, and diffraction (see Supplementary Figs. 1-3, Supplementary Table 1, and Supplementary Notes 1 and 2). The HEA nanopillar was oriented along [647] and observed close to $[1\bar{2}0]$ (Fig. 1c). Along [647], the primary and secondary slip systems are $(1\bar{1}1)[011]$ and $(1\bar{1}1)[110]$, with Schmid factors of 0.4 and 0.36, respectively. Figure 2a shows the measured stress-time curve from the as-prepared nanopillar shown in Fig. 1b. The nanopillar deformation process can be divided into three stages with: (I) little or no stress drops, (II) medium stress drops, and (III) large stress drops. In Stage I, dislocations activated from the pillar top and quickly accumulated

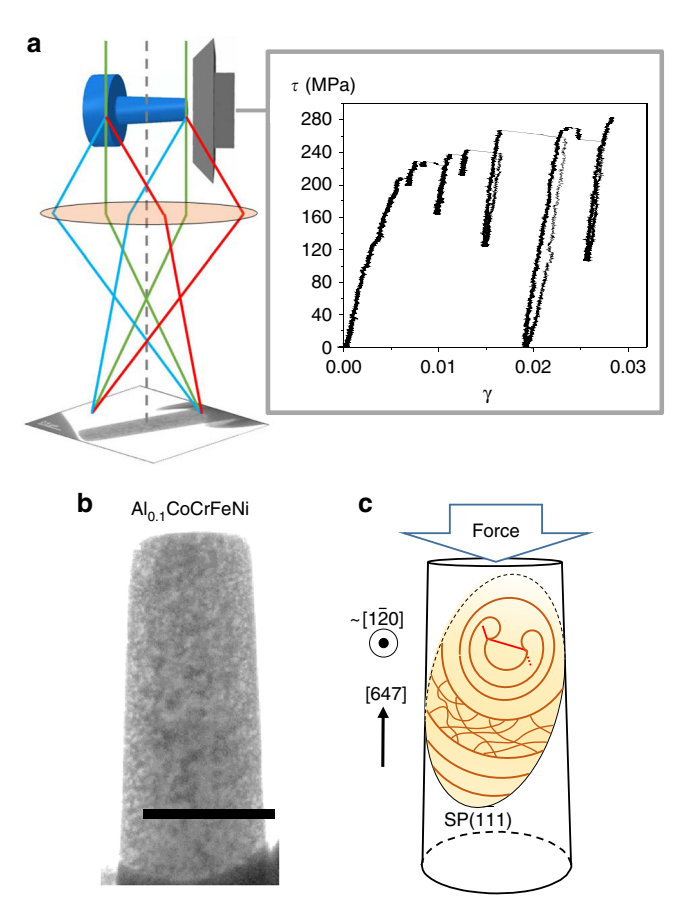


Fig. 1 The design of nanopillar compression experiment. **a** illustrates the nanopillar compression experiment as performed in a transmission electron microscopy (TEM). The electron image of the nanopillar and the stress (τ) -strain (γ) curve are simultaneously recorded as functions of time. **b** shows a bright-field (BF) image of an as-prepared high entropy alloy (HEA) nanopillar, on which the in-situ TEM experiment was carried out (scale bar is 500 nm). The image contrast indicates a relatively uniform starting dislocation microstructure. **c** presents a schematic of the nanopillar orientation and the activated slip system, $(1\bar{1}1)[0\bar{1}1]$, with a Frank-Read source under compression

forming a band of high dislocation density, which then propagated like a wave toward the pillar bottom (Fig. 2b). Stage II is characterized by small dislocation avalanches, and the resulting stress drops in the stress–strain curve. This effect is shown in Fig. 2c where a group of dislocations jumped within the camera time resolution of 0.1 s, resulting in a stress drop of 0.8 MPa. In Stage III, dislocation avalanches led to large crystal slips, as evidenced by TEM imaging (Fig. 2d), by scanning electron microscopy (SEM) (Fig. 2e) and by the correlation between the measured stress–time curve and the captured video (Supplementary Movies 1 and 2).

Avalanche size distribution. The magnitude of dislocation avalanches can be measured by the size of the nanopillar slip (S) recorded in the displacement–time curve (Fig. 3a). To examine the scaling behavior for the slip-size distributions and other statistical properties, we plot the Complementary Cumulative Distribution Function (CCDF), $C(S,\sigma)$, in Fig. 3b. The CCDF gives the probability of measuring a slip event that is larger than the size, S, at the applied stress, σ . In the mean field theory (MFT) model^{7,24}, in the absence of hardening and weakening, at a certain level of the applied stress, the slip size distribution $D(S,\sigma)$ follows a power law multiplied with an exponentially decaying

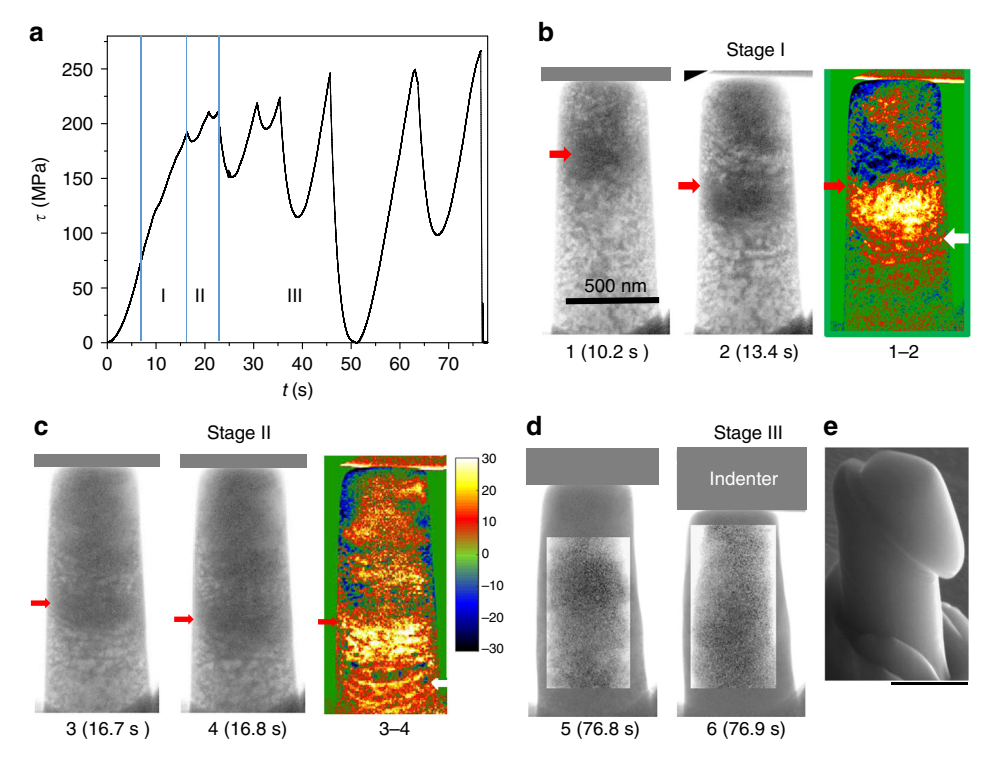


Fig. 2 In-situ nanomechanical measurement and transmission electron microscopy (TEM) observation of slip avalanches. a shows the measured stress-time curve with color-coded deformation stages (I, II, and III). b-d present two captured images at each stage, one is before and one is after a nanopillar slip. The images are labeled from 1 to 6, and their recording time is labeled below the image. Regions of the images are highlighted by red and white arrows to mark the dislocation band and the dislocation pileup. e is a scanning electron microscopy (SEM) image of the deformed nanopillar, which confirms the large crystal slips. 1–2 and 3–4 are two difference images between the images of 1 and 2, 3, and 4, respectively; they are displayed in color. The color bar marks the difference intensity level in counts. The scale bar is 500 nm. For further details, see the text

function (f_S), which limits the avalanches to be smaller than a cutoff size, $S_{\max} \sim (\sigma_c - \sigma)^{-\frac{1}{\beta}}$.

$$D(S,\sigma) \sim S^{-\kappa} f_S \left[S(\sigma_c - \sigma)^{\frac{1}{\beta}} \right].$$
 (1)

Here, S is the magnitude of the displacement jump of one slip avalanche, and σ_c is the failure stress, also called a critical stress. The MFT model predicts that $\kappa = 1.5$ and $\beta = 0.5$. The CCDF C (S,σ) is given by

$$C(S,\sigma) \sim \int_{S}^{\infty} D(S',\sigma) dS' \sim S^{-(\kappa-1)} g\Big(S(\sigma_c - \sigma)^{\frac{1}{\beta}}\Big),$$
 (2)

where $g(x) = x^{\kappa-1} \int_x^\infty e^{-At} t^{-\kappa} dt$ is a universal scaling function⁷. By introducing $f = (1 - \sigma/\sigma_c)$, the CCDF can also be evaluated as⁷,

$$C(S,f) \sim \int_{S}^{\infty} D(S',f)dS' \sim f^{\frac{(\kappa-1)}{\beta}} g_f \left(Sf^{\frac{1}{\beta}}\right).$$
 (3)

Here, $g_f(x) = \int_x^\infty e^{-At} t^{-\kappa} dt$ is another scaling function whose form was given previously⁷. With this explicit function for the slip-size distribution, a scaling collapse of the experimental slip avalanche size distribution can be used to verify the exponent values predicted by the MFT model. The log-log scaled CCDFs in Fig. 3b include 145 slip events from seven HEA nanopillars, extracted directly from the displacement-time signal (an example is shown in Fig. 3a, for details about the analysis, see Supplementary Fig. 4 and Supplementary Note 3). The measured slip sizes range from several to hundreds of nm, which were sorted into 4 categories based on the value of σ when the event occurred, from 0.6 to 1 times σ_m (where $\sigma_m = \sigma_c$ is initially taken

to be the maximum observed stress in a nanopillar). In Fig. 3c, we plot $C(S,f)f^{\frac{\kappa-1}{\beta}}$ versus $Sf^{\frac{\kappa}{\beta}}$ and we find that the rescaled CCDFs binned over all stress levels collapse onto each other, whose shape follows a universal scaling function as $g_f(x)$ with A=1.2. The critical exponents $(\sigma_m, \beta,$ and $\kappa)$ shown in the figure were tuned for the collapse. This process yielded exponents that are consistent with the predicted MFT model values, $\kappa=1.5$ and $\beta=0.5^7$.

Avalanche velocity and stress drop. In addition to the size, we also determined the avalanche velocity and stress drop from the recorded displacement– and stress–time curves, respectively. The velocity varies as shown in Fig. 3d, e. Figure 3f shows the correlation between the avalanche velocity and the applied stress, while Fig. 3g plots the stress drops and slip sizes from 4 nanopillars of different diameters. The nanopillar slips are only observed with the resolved shear stress (RSS), τ , greater than 172 MPa (Fig. 3f). Above this stress level, the avalanche velocity tends to rise with the RSS. However, the velocity is broadly distributed, as indicated by the wide range of velocities above and below the average values (Fig. 3f). The stress drop depends linearly on the observed slip size; the slope of the curve depends on the diameter of the nanopillar (Fig. 3g).

Dislocation activities during an avalanche. Figure 4 examines the dislocation activities that led to the avalanche at 16.7 s in Fig. 2a using the difference image, which is obtained by subtracting the "after" frame from the "before" frame for two consecutive video frames. The positive and negative intensities in the difference image correlate with the creation and annihilation of dislocations, as is illustrated by examples shown in Fig. 2b, c. Image 1 of Fig. 4a captures the early stage of the dislocation band

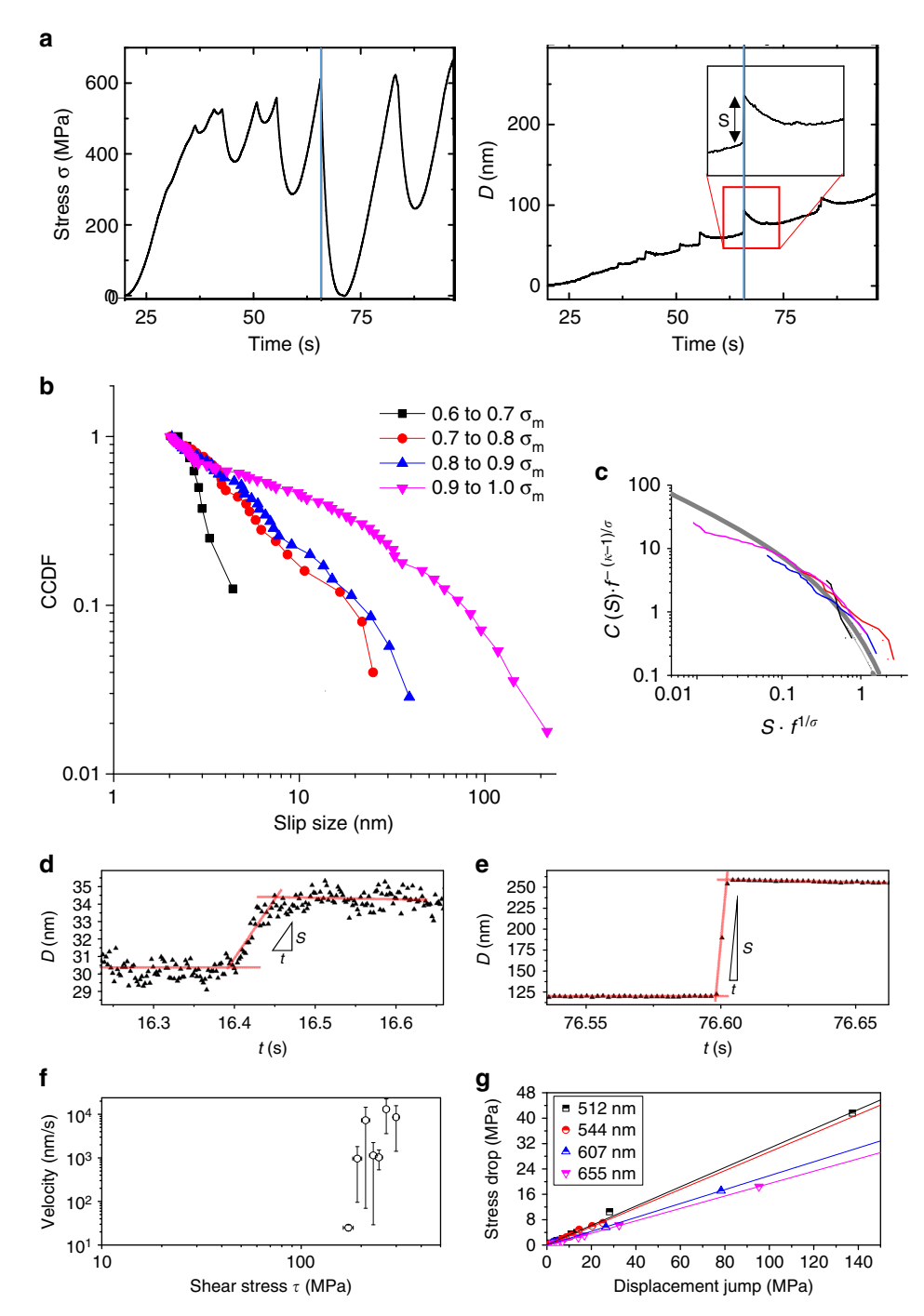


Fig. 3 Characteristics of dislocation avalanches in the Al_{0.1}CoCrFeNi nanopillars. **a** shows the characteristic stress- and displacement-time curves for the in-situ compression experiment and for a [647]-oriented nanopillar. **b** plots the stress-binned complementary cumulative distribution, $C(S, \sigma)$, of slip sizes as a function of the stress level over the maximum stress using 145 events from seven [647]-oriented samples of ~512-655 nm in diameters, compressed at a strain rate of 1 × 10⁻³/s and with similar load-displacement characteristic. **c** shows the scaling collapse of the same data as well as the predicted scaling function (see the text for details). **d**, **e** show two different types of displacement jumps. The velocity is calculated by the ratio of the displacement jump, *S*, and duration t. **f** Slip velocity as a function of shear stress. **g** Stress drop versus slip size. The avalanche velocities in (**e**) are averaged over a rolling slip size window of 2 nm, where the slip size distribution within the window is represented by the vertical bar, which marks the minimum and the maximum slip size

formation, where the bow-out of several dislocations was observed, and Image 2 reveals the formation of dislocations in front of the dislocation band, which become a dislocation pileup in Image 3. The avalanche captured in Image 5 of Fig. 4a resulted in a pillar displacement of 3.88 ± 0.17 nm at 16.7 s. The avalanche was accompanied by dislocation activities that spanned the entire pillar, including a jump of the dislocation band. It also created a

new dislocation array, as marked by the arrow in Image 5 of Fig. 4a. Intermittent dislocation activity also occurred before and after the dislocation avalanche (Images 4 and 6 in Fig. 4a), resembling a "foreshock" and an "aftershock" of an earthquake. In both cases, we observed dislocation movements in front of the dislocation band, giving rise to the nanopillar slips of 0.78 ± 0.16 and 1.01 ± 0.17 nm, respectively.

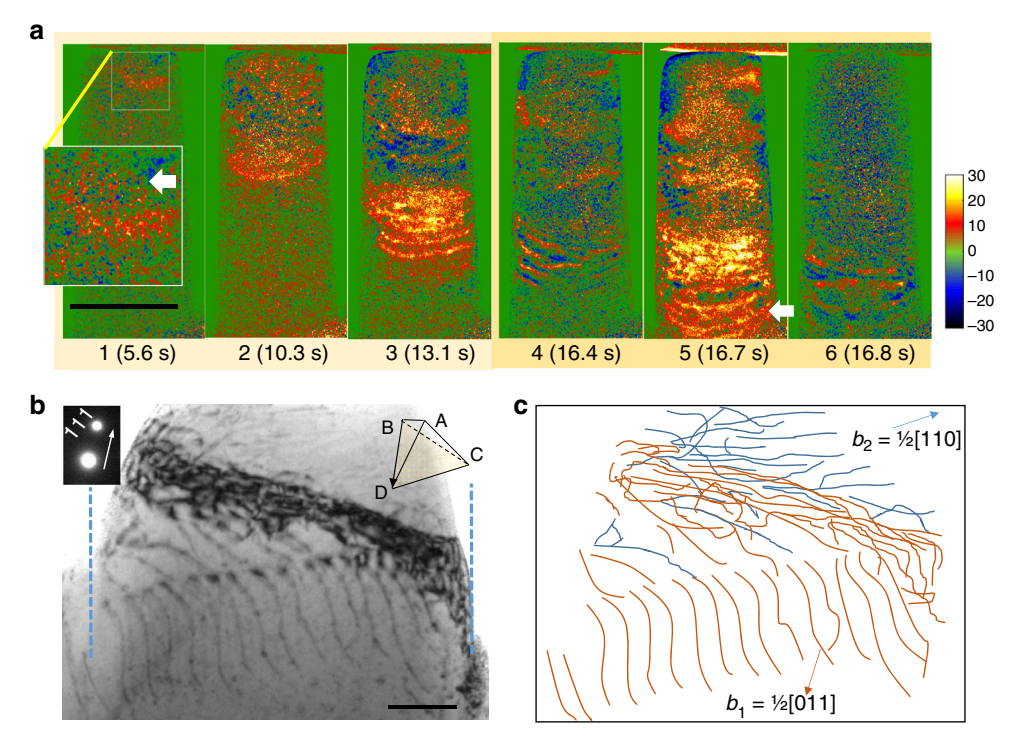


Fig. 4 The dislocation avalanche and dislocation pileup. **a** Dislocation activities leading to and after an avalanche are revealed by the difference of two consecutive images for events marked as 1-6 at the specified starting time. The color bar marks the intensity level in counts (maximum counts in an image is 255). The scale bar is 500 nm. **b** Post-mortem transmission electron microscopy (TEM) image of a deformed high entropy alloy (HEA) nanopillar recorded in bright field under the two-beam diffraction condition (inset). The nanopillar was thinned a few degrees off the normal direction of [1–20] by focused ion beam (FIB). The Thompson's tetrahedron shows the orientation of the primary slip plane (BCD, colored) relative to the electron beam. The scale bar is 100 nm. **c** A schematic illustration of dislocation characters and distribution in the sample of (**b**) compiled from images taken under different two-beam conditions. Blue dashed lines in (**b**) indicate the edge of the original nanopillar

The formation of dislocation bands. The initial yielding of the HEA nanopillars is accompanied by the dislocation multiplication through the Frank-Read or single-arm dislocation sources inside the nanopillars (see Image 1 of Fig. 4a, Supplementary Fig. 5, and Supplementary Movies 3 and 4). This situation differs from elemental fcc metals, for which dislocation starvation and strengthening are observed when the initial dislocation density is below a diameter-dependent critical value²⁵, and the mobile dislocations escape the crystal due to the image forces exerted by the surface^{6,22,23}. The accumulation and storage of dislocations in the HEA form the dislocation bands, or bundles, with the slowdown of dislocations. Post-mortem TEM characterization shows that the dislocations in the band consist of primary dislocations with b = 1/2[011] and coplanar secondary dislocations with $\mathbf{b} = 1/2[110]$, and the dislocation band is composed of mostly primary edge dislocations (Fig. 4b, c). The secondary dislocations are formed in the vicinity of the dislocation band. A rotation is also generated by the formation of a dislocation band (amounts to 3.2° in Fig. 4b). Dislocation bundles seen by ex-situ TEM have been reported before in the deformed fcc single crystals oriented for the single slip²⁶. These dislocations are known to arrange approximately in planes parallel to the slip plane. The stability of the structure under a constant applied stress is achieved through dislocation dipoles, which cancel the long-range stress. Previous studies have also identified "glide zones" in the primary slip plane near the bundles, which act as the dislocation source26,27. However, the dislocation microstructure in deformed single crystals of elemental metals is on the scale of tens to hundreds of microns. In the HEA nanopillars, we see multiple dislocation bands formed by the accumulation of dislocations. This trend has never been seen before on such a small scale.

Dislocation pileup. The experimental result in Fig. 4b confirms the dislocation pileup in front of the band. The creation of a dislocation array also indicates the operation and shut off of dislocation sources, as well the presence of obstacles that impede the front dislocation motion. Figure 5 shows the formation of a dislocation pileup in-situ. Under the applied shear stress, the mobilized part of the front dislocation bowed out (Fig. 5a). When the threshold stress was reached in Fig. 5b, the Frank-Read source(s) operated and generated a dislocation pileup, as well as a jump of the dislocation band. The restricted motion of dislocations in the pileup produced a back stress to the following dislocations and opposed the Frank-Read source operation. In the past, the existence of the dislocation pileup during crystal slip, and the related long-range internal stresses have been the subject of intense debate; evidence for their existence were only found under the special conditions of low-temperature cooling and dislocation pinning by neutron irradiation²⁶. The stress produced by the pileup in the front is proportional to the number of piled-up dislocations. Thus, a rise and fall of the local stress is expected as the pileup forms and breaks away. This trend is indeed observed by the in-situ electron diffraction (Supplementary Fig. 6 and Supplementary Note 4).

The flow of plastic deformation. To correlate intermittent dislocation activities with the laminar flow of plastic deformation and work-hardening, Fig. 6 shows a spatiotemporal map of dislocation-band propagation together with the stress–time curve. The spatiotemporal map was obtained by plotting the density of line pixels (DLP) along the pillar length direction. The line pixels represent the line features recorded in the diffraction contrast images. They are obtained by applying a line filter to the recorded

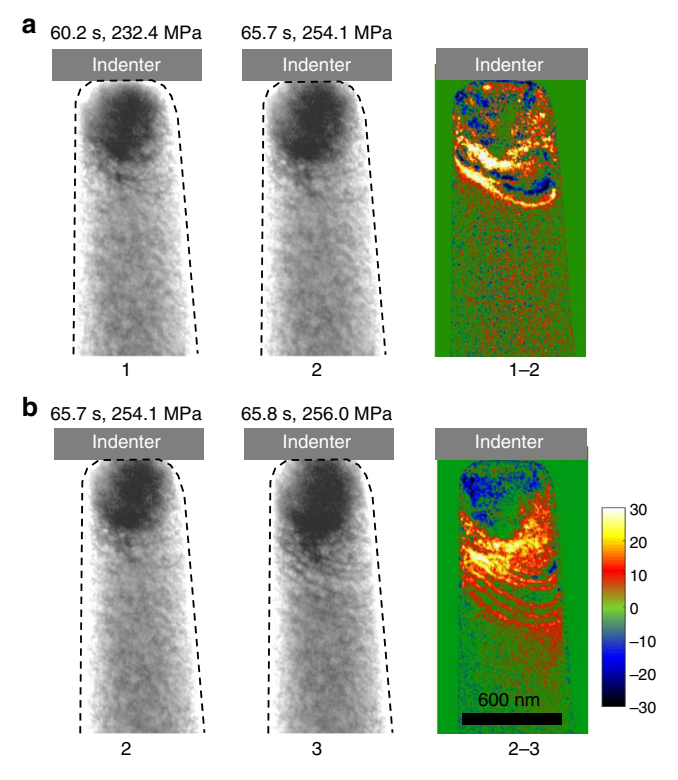


Fig. 5 The formation of dislocation pileup in front of a dislocation band. **a** shows the bowing out of the mobile part of a dislocation under the applied stress. **b** captures the Frank-Read dislocation source operation, which generated a dislocation pileup that also resulted in a sudden movement of the dislocation band, as evidenced in the difference image

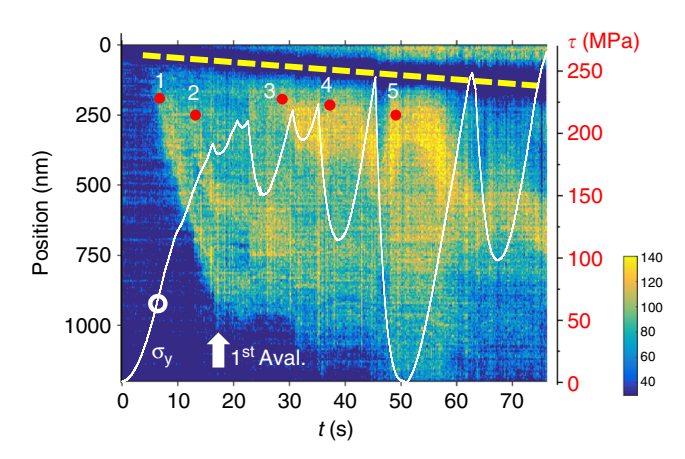


Fig. 6 Plastic flow in the nanopillar. The map shows the density of line pixels (DLP) distribution along the pillar versus time, overlapped with the stress-time curve. An example of the DLP measurement is provided in Supplementary Figure 8

images (details provided in the Methods section and in Supplementary Figs. 7, 8). Figure 6 shows the formation and propagation of multiple dislocation bands for the nanopillar measured in Fig. 2. The dislocations first activated near the nanopillar top (Supplementary Fig. 9), when the stress was below the yield strength (64 MPa) of the bulk $Al_{0.1}$ CoCrFeNi sample²⁸. This activation led to the 1st band formation, which then propagated through the nanopillar at the average velocity of ~70 nm/s and up to the distance of ~900 nm. The 2nd band started at a position lower than the 1st band and propagated by ~600 nm. The flows

of 1st and 2nd bands are relatively smooth in Stage I, but become strongly intermittent in Stages II and III. In Stage III, additional bands formed and propagated through the nanopillar. The width of the dislocation bands also changed with time.

Figure 6 also shows that the dislocation avalanche at 16.8 s occurred after the propagation of the band 1 stopped. Before the avalanche, only small dislocation movements and small slips are observed, as evidenced in Image 4 of Fig. 4a. In the HEA nanopillars, the large pillar slips occurred in Stage III. The slip sizes involved in the large displacement jumps reached about 10² nm. A notable stress drop is also associated with the slip, which corresponds to the stress released by the escaping dislocations. The large stress drops are on the order of 10² MPa.

Discussion

The avalanche mechanism that we identified for HEAs is based on interactions between the dislocation pileup and the dislocation band, and between the pileup and dislocation pinning centers. Unlike the slip of individual dislocations, which can be approximated as elastic strings of constant stiffness, the stiffness of a pileup is dependent on the long-range interactions between dislocations²⁹. Our statistical analysis shows the slip avalanche's dependence on the stress level, which indicates that the applied stress is a critical tuning parameter. Deformation of HEAs thus exhibits the tuned critical behavior rather than self-organized criticality. This result agrees with recent findings on bulk metallic glasses³⁰ and elemental metal micropillars⁷. Thus, while the avalanche mechanisms are materials specific, the avalanche distribution is universal. The distribution used in our analysis is predicted by a simple, coarse-grained, model^{7,24}. Other powerlaw distributions of different exponents and cutoff functions have been predicted^{31–33} or observed³⁴. However, a quantitative differentiation between these distributions requires a much larger slip-size range and sample size than what are measured here in the HEA nanopillars³⁵.

Lastly, we note that the demonstration of the less observable dislocation processes during the quiescent periods between avalanches was made possible by the low dislocation mobility in the HEA. To put it in perspective, the dislocation motion in elemental metals is generally very fast in single crystals of pure metals (for pure Cu, the fast velocity was measured in the range of $\sim 1-10^2$ m/s³⁶). The slip velocities, measured in the micropillars of several metals and Si using the nanoindentation techniques, are considerably less. Nonetheless, they are still quite large, from 10³ to 10⁶ nm/s³⁷. In these measurements, the dislocations involved were not observed. Thus, it was not possible to pin down the mechanism behind the dislocation motions. In a TEM, it is possible to observe and measure the speeds of individual dislocations. Previously, Kiener et al. 38 reported the dislocation speed for the individual dislocation motion at ~2.5 µm/s in the irradiated copper, where dislocations were slowed down by irradiation defects. Here, we detected two types of dislocation motions: dislocation avalanches with the slip velocities reaching 10^4 nm/s (Fig. 3f), and the slow dislocation speeds at ~ 10^1 nm/s, involving a few dislocations in front of the dislocation band even under the shear stress ~200 MPa (Supplementary Fig. 10). A critical question is thus what slows down the dislocations? A major factor that distinguishes conventional metals and the HEAs is the severe lattice distortions in HEAs, due to the atomic size variations of the constituent elements and the variations in the binding energy between atom pairs. The severe lattice distortions are expected to lead to solid-solution hardening, however, the exact nature of lattice distortions in HEAs is still unknown for the lack of suitable probes¹⁷. Our study of the HEA structure has demonstrated an inhomogeneous strain field and low angle

boundaries (Supplementary Figs. 3, 1). Local clusters of nm size are observed in the measured strain maps. The lattice distortions increase the lattice friction stress, also known as the Peierls-Nabarro (P-N) stress. A dislocation line only moves when sufficiently high stress is provided to overcome the P-N stress²⁸. Additionally, the low-angle grain boundaries are also well-known as strong dislocation barriers, which hinder the dislocation motion. Previous studies have also demonstrated that HEAs have the low stacking fault energy (SFE)^{17,18,39}. The fcc metals with the low SFE cannot easily cross slip, and hence the slip is localized on a limited set of slip planes. Together, the low SFE and the strong pinning centers contribute to the low dislocation mobility in the HEA that is critical to the formation of dislocation pileups. Thus, understanding the nature of inhomogeneous strain fields and their contribution to the plastic instability in HEAs will help the design of new and better multicomponent alloys.

Methods

Sample preparation. The Al_{0.1}CoCrFeNi HEA with a targeted composition of 2.44 at% for Al and 24.4 at% for Co, Cr, Fe, and Ni was fabricated by the Sophisticated Alloys Inc. (Butler, PA) using vacuum induction melting. The as-cast samples were hot isostatic pressed at 1100 °C for 1 h under a 207 MPa ultra-highpurity argon pressure to reduce porosity. The composition and chemical homogeneity were checked by the APT analysis (Supplementary Fig. 1 and Supplementary Movie 5). A crystal grain of hundreds µm in size, and [647] orientation was identified by electron backscattered diffraction (EBSD) and selected to produce HEA nanopillars. Nanopillar samples with diameters of 500-700 nm on a base of ~3 times wide for lift-out were fabricated and attached to the Mo lift-out grids, using a dual beam focused ion beam (FIB) and a three-step process involving the milling currents of 40 and 7 pA, 30 kV Ga ions, in the last two steps to reduce the milling damage. The milling damage was evaluated by electron diffraction, and the surface modification is <4 nm thick (Supplementary Fig. 11). The composition uniformity of the pillars was confirmed by X-ray energy dispersive spectroscopy (EDS). The pillar had a taper angle of 2.5° and aspect ratios (diameter:height) of ~1:3 to minimize the lateral constraint. This geometry provides a stable imaging condition during the compression test (the orientation of a similar nanopillar was monitored by diffraction, see Supplementary Fig. 12).

In-situ compression test. In situ compression tests of the HEA nanopillars were performed, using a picoindenter (Hysitron PI95, Hysitron, MN) equipped with a 2μm flat punch diamond indenter in a JEOL 2010 LaB6 TEM (JEOLUSA, Boston), which was operated at 200 keV. This indenter was operated with the feedback loop on. The instrument was calibrated using a flat region of the load-time curve, where we measured the standard deviation of the load and displacement at 0.1 μN and 0.56 nm, respectively. The compression tests were performed at the displacement rates of 0.5-1.5 nm/s, resulting in a strain rate of $\sim 1 \times 10^{-3}$ /s. The load, displacement, and time data were read out at 500 Hz. The stress as the pillar is compressed is peaked at the pillar top and decreases gradually towards the pillar bottom (Supplementary Fig. 13). The stated shear stress in the text is an average number calculated by $\tau = \sigma \cos \lambda \cos \phi$, where $\sigma = F/A$ with F for the applied force and A for the cross-sectional area of the nanopillar, and $\cos\lambda\cos\phi = 0.4$. A video of each test was recorded under the image condition of Supplementary Fig. 14, using a charge-coupled device (CCD) camera (Orius CCD Camera, Gatan, Pleasanton, CA) with a resolution of 720 × 480 pixels and readout at 10 frames per second. The pillar slip was measured by the nanoindenter and by fitting the intensity profile of the indenter edge as recorded in the TEM image. (The edge position can be determined with a standard deviation of 0.26 nm.) To contrast the dislocation activities in the HEA nanopillars, we also observed the dislocation activities in a compressed Cu nanopillar (Supplementary Fig. 15 and Supplementary Movie 6).

Measurement of dislocation activities. We measured the dislocation activities by quantifying the dislocation line contrast in the recorded images, using a line detection algorithm. The recorded BF-TEM images were transformed into binary images, where the contrast of a dislocation yields a line pixel with the value of 1 (examples are shown in Supplementary Fig. 7). By counting the number of line pixels along the pillar diameter and the total number of line pixels, we gained the information about the dislocation bands as well as the intermittent dislocation activities. Using the same method, we also quantified the initial dislocation density of a HEA nanopillar (Supplementary Fig. 16).

Data availability

Data that support the findings of this study are available from the authors on reasonable request.

Received: 13 September 2017 Accepted: 7 September 2018 Published online: 01 October 2018

References

- Weiss, J., Lahaie, F. & Grasso, J. R. Statistical analysis of dislocation dynamics during viscoplastic deformation from acoustic emission. *J. Geophys. Res.: Solid Earth* 105, 433–442 (2000).
- Miguel, M. C., Vespignani, A., Zapperi, S., Weiss, J. & Grasso, J. R. Intermittent dislocation flow in viscoplastic deformation. *Nature* 410, 667–671 (2001).
- Uchic, M. D., Shade, P. A. & Dimiduk, D. M. Plasticity of micrometerscale single crystals in compression. *Annu. Rev. Mater. Res.* 39, 361–386 (2009)
- Dimiduk, D. M., Woodward, C., LeSar, R. & Uchic, M. D. Scale-free intermittent flow in crystal plasticity. Science 312, 1188–1190 (2006).
- Zaiser, M. et al. Strain bursts in plastically deforming molybdenum micro- and nanopillars. *Philos. Mag.* 88, 3861–3874 (2008).
- Brinckmann, S., Kim, J.-Y. & Greer, J. R. Fundamental differences in mechanical behavior between two types of crystals at the nanoscale. *Phys. Rev. Lett.* 100, 155502 (2008).
- Friedman, N. et al. Statistics of dislocation slip avalanches in nanosized single crystals show tuned critical behavior predicted by a simple mean field model. *Phys. Rev. Lett.* 109, 095507 (2012).
- Hirsch, P., Howie, A., Nicolson, R. B., Pashley, D. W. & Whelan, M. J. Electron Microscopy of Thin Crystals (Robert E. Krieger Publishing Company, 1977).
- Spence, J. C. H. Chapter 77 Experimental studies of dislocation core defects. Dislocations Solids 13, 419–452 (2007).
- Messerschmidt, U. Dislocation Dynamics During Plastic Deformation (Springer, 2010).
- Kubin, L. P. Dislocation patterning. In Treatise in Materials Science and Technology, Vol. 6 (ed Mughrabi, H.) 138 (VCH, D-Weinberg, 1993).
- Basinski, Z. S. & Basinski, S. J. Fundamental aspects of low amplitude cyclic deformation in face-centred cubic crystals. *Prog. Mater. Sci.* 36, 89–148 (1992).
- Brown, L. M. Constant intermittent flow of dislocations: central problems in plasticity. Mater. Sci. Technol. 28, 1209–1232 (2012).
- Csikor, F. F., Motz, C., Weygand, D., Zaiser, M. & Zapperi, S. Dislocation avalanches, strain bursts, and the problem of plastic forming at the micrometer scale. *Science* 318, 251–254 (2007).
- Yeh, J. W. et al. Nanostructured high-entropy alloys with multiple principal elements: novel alloy design concepts and outcomes. Adv. Eng. Mater. 6, 299–303 (2004).
- Cantor, B., Chang, I. T. H., Knight, P. & Vincent, A. J. B. Microstructural development in equiatomic multicomponent alloys. *Mater. Sci. Eng. A* 213–218, 375–377 (2004).
- Zhang, Y. et al. Microstructures and properties of high-entropy alloys. Prog. Mater. Sci. 61, 1–93 (2014).
- Miracle, D. B. & Senkov, O. N. A critical review of high entropy alloys and related concepts. Acta Mater. 122, 448–511 (2017).
- Gludovatz, B. et al. A fracture-resistant high-entropy alloy for cryogenic applications. Science 345, 1153–1158 (2014).
- Carroll, R. et al. Experiments and model for serration statistics in low-entropy, medium-entropy, and high-entropy alloys. Sci. Rep. 5, 16997 (2015).
- Okamoto, N. L., Yuge, K., Tanaka, K., Inui, H. & George, E. P. Atomic displacement in the CrMnFeCoNi high-entropy alloy—a scaling factor to predict solid solution strengthening. AIP Adv. 6, 125008 (2016).
- Shan, Z. W., Mishra, R. K., Asif, S. A. S., Warren, O. L. & Minor, A. M. Mechanical annealing and source-limited deformation in submicrometrediameter Ni crystals. *Nat. Mater.* 7, 115–119 (2008).
- Greer, J. R. & Nix, W. D. Nanoscale gold pillars strengthened through dislocation starvation. *Phys. Rev. B* 73, 245410 (2006).
- Dahmen, K. A., Ben-Zion, Y. & Uhl, J. T. Micromechanical model for deformation in solids with universal predictions for stress-strain curves and slip avalanches. *Phys. Rev. Lett.* 102, 175501 (2009).
- El-Awady, J. A. Unravelling the physics of size-dependent dislocationmediated plasticity. Nat. Commun. 6, 5926 (2015).
- Mughrabi, H. Comment on 'Constant intermittent flow of dislocations: central problems in plasticity' by L. M. Brown. *Mater. Sci. Technol.* 30, 123–126 (2014).
- Steeds, J. W. Dislocation arrangement in copper single crystals as a function of strain. Proc. R. Soc. Lond. Ser. A Math. Phys. Sci. 292, 343 (1966).
- Komarasamy, M., Kumar, N., Mishra, R. S. & Liaw, P. K. Anomalies in the deformation mechanism and kinetics of coarse-grained high entropy alloy. *Mater. Sci. Eng. A* 654, 256–263 (2016).

- Moretti, P., Miguel, M. C., Zaiser, M. & Zapperi, S. Depinning transition of dislocation assemblies: pileups and low-angle grain boundaries. *Phys. Rev. B* 69, 214103 (2004).
- Antonaglia, J. et al. Tuned critical avalanche scaling in bulk metallic glasses. Sci. Rep. 4, 4382 (2014).
- Zaiser, M. Scale invariance in plastic flow of crystalline solids. Adv. Phys. 55, 185–245 (2006).
- Lin, J., Lerner, E., Rosso, A. & Wyart, M. Scaling description of the yielding transition in soft amorphous solids at zero temperature. *Proc. Natl. Acad. Sci.* USA 111, 14382–14387 (2014).
- 33. Le Doussal, P., Middleton, A. A. & Wiese, K. J. Statistics of static avalanches in a random pinning landscape. *Phys. Rev. E* **79**, 050101 (2009).
- Hatano, T., Narteau, C. & Shebalin, P. Common dependence on stress for the statistics of granular avalanches and earthquakes. *Sci. Rep.* 5, 12280 (2015).
- Budrikis, Z., Castellanos, D. F., Sandfeld, S., Zaiser, M. & Zapperi, S. Universal features of amorphous plasticity. *Nat. Commun.* 8, 15928 (2017).
- Jassby, K. M. & Vreeland, T. An experimental study of the mobility of edge dislocations in pure copper single crystals. *Philos. Mag. J. Theor. Exp. Appl. Phys.* 21, 1147–1168 (1970).
- Sparks, G., Phani, P. S., Hangen, U. & Maaß, R. Spatiotemporal slip dynamics during deformation of gold micro-crystals. Acta Mater. 122, 109–119 (2017).
- 38. Kiener, D., Hosemann, P., Maloy, S. A. & Minor, A. M. In situ nanocompression testing of irradiated copper. *Nat. Mater.* **10**, 608 (2011).
- Zaddach, A. J., Niu, C., Koch, C. C. & Irving, D. L. Mechanical properties and stacking fault energies of NiFeCrCoMn high-entropy alloy. *JOM* 65, 1780–1789 (2013).

Acknowledgements

The work was supported by the Department of Energy (Grant nos. DEFG02-01ER45923 to J.M.Z., DEFE0024054 and DEFE0011194 to K.A.D. and P.K.L.) and the U.S. National Science Foundation (Grant nos. DMR-1410596 to J.M.Z., DMR 10-05209 and CBET 1336634 to K.A.D., DMR1611180 to P.K.L.). APT was conducted at the Oak Ridge National Laboratory Center for Nanophase Materials Sciences (CNMS), which is a DOE BES user facility.

Author contributions

The TEM measurements were carried out by H.Y. Q.Y. and W.G. helped with ex-situ TEM and APT characterization. The TEM data were analyzed and interpreted by H.Y. and J.M.Z. L.S. and K.A.D. contributed to the slip data analysis/theory, and P.K.L. provided the HEA sample. J.M.Z. directed the research.

Additional information

 $\label{eq:supplementary} \textbf{Supplementary information} \ \text{accompanies this paper at https://doi.org/10.1038/s42005-018-0062-z.}$

Competing interests: The authors declare no competing interests.

Reprints and permission information is available online at http://npg.nature.com/reprintsandpermissions/

Publisher's note: Springer Nature remains neutral with regard to jurisdictional claims in published maps and institutional affiliations.

Open Access This article is licensed under a Creative Commons Attribution 4.0 International License, which permits use, sharing,

adaptation, distribution and reproduction in any medium or format, as long as you give appropriate credit to the original author(s) and the source, provide a link to the Creative Commons license, and indicate if changes were made. The images or other third party material in this article are included in the article's Creative Commons license, unless indicated otherwise in a credit line to the material. If material is not included in the article's Creative Commons license and your intended use is not permitted by statutory regulation or exceeds the permitted use, you will need to obtain permission directly from the copyright holder. To view a copy of this license, visit http://creativecommons.org/licenses/by/4.0/.

© The Author(s) 2018